Correlated diffusion in lipid bilayers

Rafael L. Schoch[a,1], Frank L. H. Brown[b,c,1], and Gilad Haran[a,1]

[a]Department of Chemical and Biological Physics, Weizmann Institute of Science, Rehovot 7610001, Israel; [b]Department of Chemistry and Biochemistry, University of California, Santa Barbara, CA 93106; and [c]Department of Physics, University of California, Santa Barbara, CA 93106

Edited by Steven G. Boxer, Stanford University, Stanford, CA, and approved October 12, 2021 (received for review July 19, 2021)

Lipid membranes are complex quasi–two-dimensional fluids, whose importance in biology and unique physical/materials properties have made them a major target for biophysical research. Recent single-molecule tracking experiments in membranes have caused some controversy, calling the venerable Saffman–Delbrück model into question and suggesting that, perhaps, current understanding of membrane hydrodynamics is imperfect. However, single-molecule tracking is not well suited to resolving the details of hydrodynamic flows; observations involving correlations between multiple molecules are superior for this purpose. Here dual-color molecular tracking with submillisecond time resolution and submicron spatial resolution is employed to reveal correlations in the Brownian motion of pairs of fluorescently labeled lipids in membranes. These correlations extend hundreds of nanometers in freely floating bilayers (black lipid membranes) but are severely suppressed in supported lipid bilayers. The measurements are consistent with hydrodynamic predictions based on an extended Saffman–Delbrück theory that explicitly accounts for the two-leaflet bilayer structure of lipid membranes.

membrane hydrodynamics | Saffman–Delbrück model | single-molecule tracking

Lipid bilayer membranes are widely studied systems, not only because of their obvious biological importance (1, 2) but also due to their unusual structural, material, and dynamic properties (3, 4). From the dynamic perspective, as was first recognized by Saffman and Delbrück (SD) (5, 6), lipid bilayers behave as quasi–two-dimensional (quasi-2D) (7) fluids. Lipids and other membrane components are confined to move in a thin, essentially 2D sheet, but that sheet exchanges momentum with the surrounding fluid in 3D. For a flat membrane in an infinite bulk fluid (the canonical SD geometry), this leads to a characteristic length scale, $L_{SD} = \eta_b/2\eta_f$, affecting membrane hydrodynamics. Here $\eta_b = 2\eta_m$ is the bilayer surface viscosity (twice that of a single monolayer; note that surface viscosity carries an extra factor of length relative to traditional 3D viscosity), and η_f is the viscosity of the 3D fluid surrounding the membrane. $L_{SD} \approx 100$ to $1{,}000$ nm for typical lipid bilayers in water (6) and represents a crossover point for hydrodynamic interactions in the membrane. Membrane positions separated by less than L_{SD} interact through flows in the membrane itself, whereas distant positions interact through flows in the surrounding bulk (8). This crossover has interesting practical consequences. For example, the diffusion constant, D, for small objects in the membrane (with radius $<<L_{SD}$; e.g., lipids and proteins) displays only a logarithmic dependence on object size (6), whereas large objects (with radius $>>L_{SD}$; e.g., μm-scale lipid domains) exhibit the $D \sim 1/\text{radius}$ Stokes–Einstein-like (9) scaling found in 3D systems (10).

The original SD model assumes an infinite planar membrane immersed in an infinite bulk fluid; the membrane itself is treated as a structureless thin sheet, ignoring the dual leaflet bilayer structure. Various generalizations that relax the assumptions of the original SD model have been developed to allow for the study of supported bilayers (8, 11–13), vesicles (14), periodic membranes (as in molecular simulations) (15), immobile inclusions in the membrane (16), and two-leaflet structures (14, 17) while still retaining a continuum/hydrodynamic-level description. These generalizations build upon the underlying SD picture in relatively straightforward ways from the theoretical perspective, but they can completely disrupt the predictions of the original SD model, a fact that has led to some confusion in the literature (18). For example, supported membranes experience a strong drag from the underlying substrate, leading to the suppression of hydrodynamic interactions for separations beyond $L_{sub} = \sqrt{L_{SD}h}$ (h is the height of the membrane above the solid support) and substantially reduced diffusivities relative to a freely floating membrane (11). Self-diffusion in periodic membranes does not converge to traditional SD predictions until the box size exceeds L_{SD} in all three dimensions, an inconvenient complication for those hoping to determine D for membrane components via detailed molecular simulations (15).

The SD model was originally developed to predict self-diffusion coefficients for small membrane-spanning objects (i.e., integral membrane proteins) (6). Given this history and the relative ease of measuring membrane protein self-diffusion (19), it is perhaps unsurprising that the vast majority of experiments testing the SD theory (and its various generalizations) focus on self-diffusion coefficients. Unfortunately, the single-particle tracking (SPT) literature on this subject is controversial, with various studies claiming either success (20–22) or failure (23–25) of SD predictions for integral membrane protein self-diffusion. While it is easy to dismiss the apparent

Significance

Dynamic processes on membrane surfaces are essential for biological function. Traditionally, quantitative measurements of lipid/protein motion have been interpreted in the framework of membrane hydrodynamics. However, some recent single-molecule tracking studies have proven difficult to interpret via hydrodynamic arguments. Does this suggest a failure of hydrodynamic theory or simply highlight the dangers in attempting to extend hydrodynamic arguments down to molecular scales? Intermolecular correlations are superior to single-molecule observations for studying hydrodynamics due to the longer length scales involved. The current work reports dynamic pair correlations of lipids in model membranes. Submicron distance-dependent correlations are well resolved, and complementary numerical calculations indicate that hydrodynamic theory can predict membrane dynamics over distances of tens of nanometers and longer.

Author contributions: R.L.S., F.L.H.B., and G.H. designed research; R.L.S. performed research; F.L.H.B. contributed new reagents/analytic tools; R.L.S., F.L.H.B., and G.H. analyzed data; and R.L.S., F.L.H.B., and G.H. wrote the paper.

The authors declare no competing interest.

This article is a PNAS Direct Submission.

[1]To whom correspondence may be addressed. Email: rafael.schoch@weizmann.ac.il, flbrown@ucsb.edu, or gilad.haran@weizmann.ac.il.

This article contains supporting information online at http://www.pnas.org/lookup/suppl/doi:10.1073/pnas.2113202118/-/DCSupplemental.

Published November 23, 2021.

failures as stemming from the ill-advised application of hydrodynamic theory down to molecular scales (22–24, 26), a far more satisfactory resolution would be achieved by directly testing the performance of SD-like hydrodynamic models via measurements that are less sensitive to molecular-level details.

Two-particle microrheology measures hydrodynamic interactions via the correlated thermal motions of particle pairs (27). Unlike self-diffusion, hydrodynamic interactions are quite insensitive to the size and shape of probe particles, so long as one confines measurements to probe separations larger than the probe size (27–29). Furthermore, measurement of probe correlations over a wide range of separations provides a far more detailed test of hydrodynamic predictions than is possible via comparison to a single (or few) self-diffusion coefficient. For these reasons, it would be highly desirable to perform two-particle microrheology (or similar) measurements in lipid bilayer systems as a stringent test of SD and related hydrodynamic theories. One recent study has investigated the correlated motion of membrane proteins in neuronal cell membranes (30). However, this study involved intact living cells where all manner of complications are expected to influence protein motion. Although protein–protein correlations were observed, it proved impossible to explain them via hydrodynamic theory.

Correlated Brownian motions in model lipid membranes are expected to decay slowly (logarithmically and algebraically) but with weak amplitudes that necessitate measurements on the μm scale or shorter. Further, the rapid motion of particles in such membranes averages their positions during the measurement and complicates analysis of correlations. This work introduces the methodology necessary to overcome these difficulties. In particular, SPT with submillisecond time resolution is developed and combined with a theoretical analysis that explicitly accounts for the finite experimental acquisition times. This allows the measurement of correlated Brownian motion of lipid pairs as a function of distance in model lipid bilayers. In particular, two differently labeled lipids are tracked within freely floating black lipid membranes (BLMs) as well as within supported lipid bilayers (SLBs; Fig. 1). Using two colors allows for the study of lipid pairs with arbitrarily small interparticle distances, limited only by localization precision rather than optical diffraction. The experimental measurements are compared to an SD-like hydrodynamic model (18, 31) that accounts for the dual leaflet nature of the bilayers in both the BLM and SLB geometries. It is found that experiment and theoretical predictions are in good agreement.

Results

Preliminaries. It is well known that hydrodynamic interactions between particles in a fluid lead to correlations in the Brownian motion of these particles (9). For two particles in the creeping flow hydrodynamic regime appropriate to this work (32), both these correlations and the single-particle thermal fluctuations associated with self-diffusion are conveniently summarized by the two-body diffusion matrix, $\boldsymbol{D}(\boldsymbol{r}_{12})$. In the membrane geometry relevant to this work, the distinct elements of the diffusion matrix are ($\ell = 1,2$ indexes the two particles, and $\alpha = +,-$ indexes the two leaflets of the bilayer)

$$D_\ell^\alpha = \frac{1}{2\Delta\tau}\langle(\Delta x_\ell)^2\rangle = \frac{1}{2\Delta\tau}\langle(\Delta y_\ell)^2\rangle, \quad [1a]$$

$$D_L^\alpha(r_{12}) = \frac{1}{2\Delta\tau}\langle(\Delta x_1)(\Delta x_2)\rangle, \quad [1b]$$

$$D_T^\alpha(r_{12}) = \frac{1}{2\Delta\tau}\langle(\Delta y_1)(\Delta y_2)\rangle, \quad [1c]$$

where Δx_ℓ and Δy_ℓ are longitudinal (in the direction of the particle separation vector, $\boldsymbol{r}_{12}$) and transverse (perpendicular to the particle separation vector) probe displacements, respectively, over a short displacement time $\Delta\tau$ [short enough to insure that the associated displacements do not change r_{12} enough to significantly alter the elements of $\boldsymbol{D}(\boldsymbol{r}_{12})$]. The angular brackets indicate an averaging over the random Brownian behavior associated with two particles initially separated by $\boldsymbol{r}_{12}$ but otherwise at thermal equilibrium. D_ℓ^α is the usual self-diffusion constant for lipid ℓ when it is located in leaflet α. [Although D_ℓ^α could depend in principle upon $\boldsymbol{r}_{12}$, this dependence is very weak except for separations comparable to particle size (31) and will not be considered in this work.] $D_L^\alpha(r_{12})$ and $D_T^\alpha(r_{12})$ quantify correlations in the diffusive motion between particles 1 and 2. These correlations derive from hydrodynamic flows in the membrane and surrounding fluids; correlation is strongest for particles that are proximal to one another and falls off as the particles separate. One might also consider $D_{L(T)}^{\alpha\beta}(r_{12})$, which reports on correlations between lipids in opposing leaflets; however, such measurements are more challenging from the experimental perspective and are not considered in this work.

It is stressed from the outset that technical limitations preclude the direct experimental determination of $D_{L(T)}^\alpha(r_{12})$ from Eqs. **1b** and **1c**. Experimentally realizable time scales are not sufficiently short to hold $\boldsymbol{r}_{12}$ nearly constant. (This issue is irrelevant to the measurement of self-diffusion coefficients since D_ℓ^α is independent of $\boldsymbol{r}_{12}$; Eq. **1a** is valid for arbitrarily large $\Delta\tau$.) So, while Eqs. **1b** and **1c** motivate the measurements described in *Measuring and Analyzing Lipid Motion*, a quantitative analysis of these measurements requires more elaborate theoretical

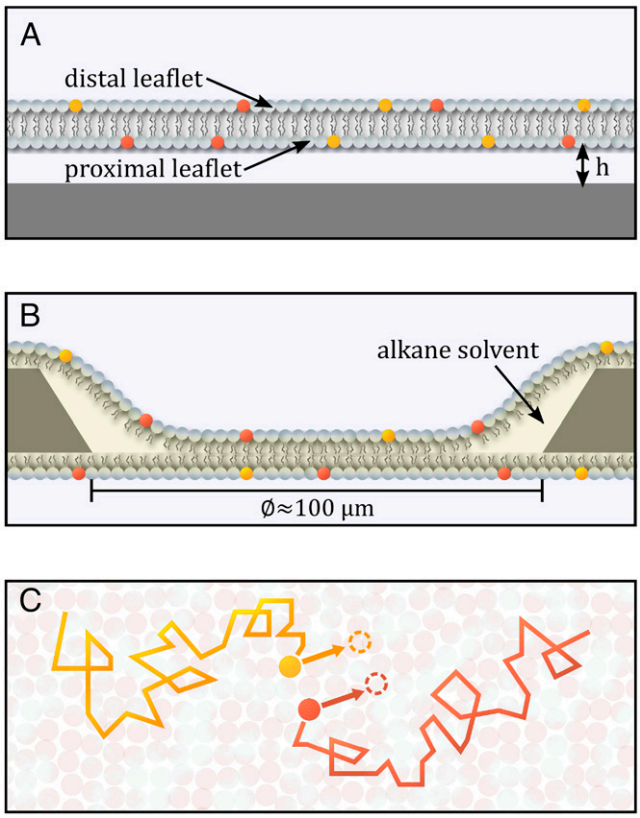

Fig. 1. Model lipid bilayer systems used to study correlated Brownian motion. (Cartoons not to scale.) The labeled probes for SPT are shown in orange and red. (*A*) SLB formed on a microscope cover glass. The height of the membrane above the solid support, h, is ~1 nm. (*B*) BLM formed on a μm-sized aperture. (*C*) Probe trajectories for a pair of labeled lipids. The arrows indicate correlated motion of the probes.

considerations than might be naïvely expected. A description of the required quantitative analysis follows in *Hydrodynamics and Lipid Diffusion in Two-Leaflet Membranes*.

Measuring and Analyzing Lipid Motion. Two-color SPT experiments of fluorescently labeled lipid probes embedded in SLBs and BLMs formed from egg L-α-phosphatidylcholine (EPC) were performed, using a home-built total internal reflection microscope (*Methods* and *SI Appendix, Methods*). Simultaneous diffusive trajectories of red and orange labeled lipid probes (Atto647N- and Atto550-labeled DMPE, henceforth "lipid 1" and "lipid 2," respectively) were obtained by localizing single molecules in individual camera frames and linking them in consecutive frames (33). It is essential to note that lipid molecules embedded in a membrane move a considerable distance during the experimental frame time of $t_f = 7.76$ ms. For example, the BLM lipids studied here have self-diffusion coefficients on the order of $D \approx 10\ \mu m^2/s$ (see below), leading to an rms displacement of $\langle \Delta r^2 \rangle^{1/2} = \sqrt{4Dt_f} \approx 500$ nm in each frame. Attempting to infer μm-scale hydrodynamic correlations based upon frame-averaged lipid positions that are inherently uncertain to within half a μm is a dubious proposition at best. To partially mitigate this problem, camera-synchronized excitation pulses were used to obtain effective frame times much smaller than t_f (34). The method is illustrated in Fig. 2 *A* and *B*, showing pairs of excitation pulses grouped around every second dead time period between camera frames ($\Delta t_{off} = 290$ μs). In the SLB experiments, the excitation pulses have a length of $\Delta t_{on} = 350$ μs. This leads to alternating displacement time intervals $\Delta t_{short} = 640$ μs and $\Delta t_{long} = 14.9$ ms. A high laser intensity of $\sim 5 \times 10^3$ W/cm^2 was used in order to obtain high-enough signals during the short illumination times. Yet, the long dark time between pairs of pulses allowed sufficient probes to diffuse into the imaging area without being photobleached. BLM experiments were performed using an epi-illumination mode, so that for the same nominal laser intensity the actual excitation intensity was lower by a factor of ~2 to 3. Therefore, longer pulses $\Delta t_{on} = 1,210$ μs were used such that $\Delta t_{short} = 1.5$ ms.

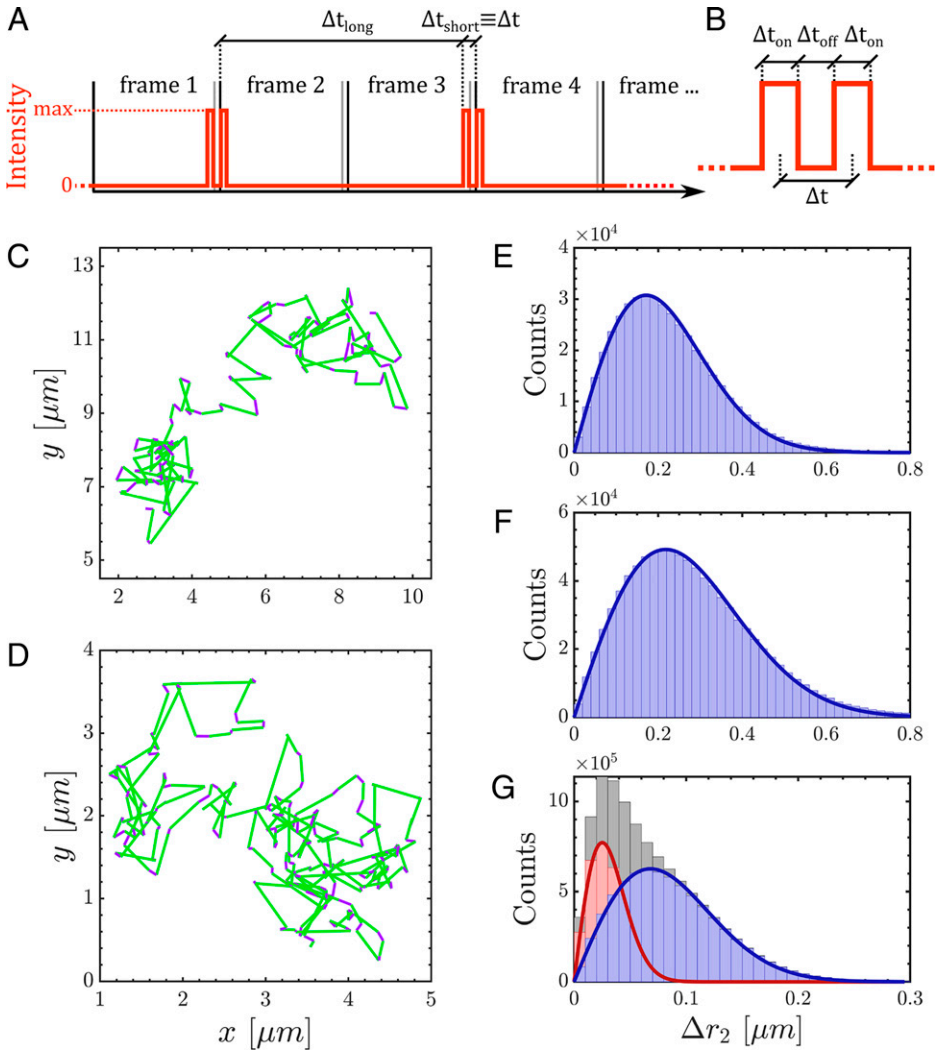

Fig. 2. Measuring and analyzing lipid motion. (*A*) The illumination pulsing scheme consists of pairs of laser pulses grouped around every second dead time period between camera frames. This leads to short displacement times Δt_{short} alternating with long ones Δt_{long}. Motion was analyzed based exclusively on $\Delta t \equiv \Delta t_{short}$. (*B*) Zoom in on a pair of laser pulses of length Δt_{on} separated by a dark time of length Δt_{off}. Δt_{on} is the time window over which lipid positions $\boldsymbol{r}_\ell(t)$ are measured, and $\Delta t = \Delta t_{on} + \Delta t_{off}$ is the interval over which lipid displacements are inferred as the difference between two successive position measurements. (*C*) Sample trajectory $\boldsymbol{r}_2(t)$ of an Atto550-DMPE probe in BLM_h, obtained using illumination pulsing. The displacements based on Δt are shown in blue. (*D*) Same as *C* but for the SLB case. (*E*) Distribution of scalar displacements Δr_2 based on Δt in BLM_h. (*F*) Same as *E* but for BLM_d. (*G*) Same as *E* but for an SLB. Gray shows full distribution, and red and blue show slow and fast populations, respectively, obtained from a two-state HMM analysis of the trajectories. Continuous lines are fits.

Full trajectories obtained using illumination pulsing are shown in Fig. 2 *C* and *D* for the SLB and BLM cases. Analysis of self-diffusion and correlated diffusion relies only on the lipid vector displacements ($\Delta \boldsymbol{r}_\ell$) observed between adjacent "on" pulses with $\Delta t_{short} = 640$ μs for the SLB and $\Delta t_{short} = 1.5$ ms for the BLM cases (indicated by the blue segments in Fig. 2 *C* and *D*). For the remainder of the paper, therefore, the notation $\Delta t_{short} \equiv \Delta t$ is used for simplicity.

Measurements in BLMs were performed on lipid probes diffusing in one leaflet only, which was achieved by quenching probes in the other leaflet using iodide ions. Distributions of the scalar displacements $\Delta r_2 = |\,\Delta \boldsymbol{r}_2\,|$ for Atto550-DMPE (i.e., lipid probe $\ell = 2$) are shown in Fig. 2 *E* and *F* for BLMs formed from a *n*-hexadecane solution or from an *n*-decane solution, designated BLM_h and BLM_d, respectively. These distributions are unimodal. In contrast, trajectories collected from SLBs demonstrate bimodal lipid dynamics with two populations, fast and slow, as shown in Fig. 2*G*. The two populations of molecules were distinguished using a two-state hidden Markov model (HMM) analysis (33). As shown previously using iodide quenching (33), the slow and fast diffusive modes are associated with the proximal and distal leaflets of the SLB, respectively.

Fitting the distributions in Fig. 2 (and similar distributions for Atto647N-DMPE) to the appropriate expression (*SI Appendix*, *Single-Particle Tracking*) yields the self-diffusion coefficients. For BLM_h, $D_1 = 13.6 \pm 0.3\ \mu m^2/s$ and $D_2 = 13.0 \pm 0.3\ \mu m^2/s$, while for BLM_d, $D_1 = 20.6 \pm 0.4\ \mu m^2/s$ and $D_2 = 20.5 \pm 0.5\ \mu m^2/s$. Due to the symmetry of BLMs, these values are the same in both leaflets. Clearly, the diffusion is slower in BLM_h than in BLM_d, which is in agreement with the trend of slower diffusion with increasing *n*-alkane chain length reported previously (35). The two different probes share the same diffusivities to within experimental uncertainty. By fitting the two distributions of Δr_2 calculated from SLB data (Fig. 2*G*), diffusion coefficients $D_2^- = 0.08 \pm 0.05\ \mu m^2/s$ and $D_2^+ = 4.27 \pm 0.13\ \mu m^2/s$ for Atto550-DMPE are obtained; $D_1^- = 0.13 \pm 0.06\ \mu m^2/s$ and $D_1^+ = 4.01 \pm 0.06\ \mu m^2/s$ for Atto647N-DMPE are obtained similarly. The diffusivities in the proximal/distal ($^{+/-}$) leaflet are very different, but again the numbers are relatively insensitive to the identity of the lipid probe.

The diffusive trajectories collected for Atto647N-DMPE and Atto550-DMPE were also used to determine the experimental correlations between lipids. For each Δt separated pair of pulses and for each distinct 1,2 pair of lipids, the coordinate frame was rotated to set the *x* axis along the first-pulse $\boldsymbol{r}_{12}$ (Fig. 3*A*). The longitudinal and transverse probe displacements between consecutive excitation pulses of probe $\ell = 1, 2$ are then Δx_ℓ and Δy_ℓ, respectively. The use of two colors allowed for the study of lipid pairs with arbitrarily small interparticle distances r_{12}, unlimited by optical diffraction. Experimental longitudinal and transverse correlations were then determined by averaging

$$c_L(r_{12}) = \frac{\langle \Delta x_1 \Delta x_2 \rangle_r}{2\Delta t}, \qquad [2a]$$

$$c_T(r_{12}) = \frac{\langle \Delta y_1 \Delta y_2 \rangle_r}{2\Delta t}, \qquad [2b]$$

where $\langle \cdots \rangle_r$ denotes averaging only over pairs separated by a distance r_{12} in the first pulse. The probe positions and displacements shown in Fig. 3*A* depict an ideal experiment in terms of spatiotemporal resolution. In contrast, in a real experiment, it is the center of mass of the emission pattern of a fluorescent lipid collected during Δt_{on} that is measured and assigned to $\boldsymbol{r}_\ell(t)$, as depicted in Fig. 3*B*. It follows that a probe pair effectively samples a distribution of separation vectors $\boldsymbol{r}_{12}$ while recording the displacements $\Delta \boldsymbol{r}_\ell(\Delta t)$. Even though the pulsing scheme serves to improve the spatiotemporal resolution, there is still significant lipid motion during the finite Δt. This needs to be considered when comparing the experimental correlations with theoretical predictions, as will be detailed in *Hydrodynamics and Lipid Diffusion in Two-Leaflet Membranes*.

Hydrodynamics and Lipid Diffusion in Two-Leaflet Membranes. The results presented below involve quantitative comparisons between experimental data and hydrodynamic predictions for the behavior of lipids diffusing in bilayer membranes. The underlying hydrodynamic model (18, 33) used for these comparisons should be viewed as the natural extension of the venerable SD model to membranes with a two-leaflet structure (14, 17) and (in the case of SLBs) an underlying solid support (8, 11–13). A two-leaflet description is required since the lipid probes do not span the entire membrane but reside in a single monolayer. Fig. 3*C* provides a cartoon illustrating the underlying physics. The membrane is modeled as two

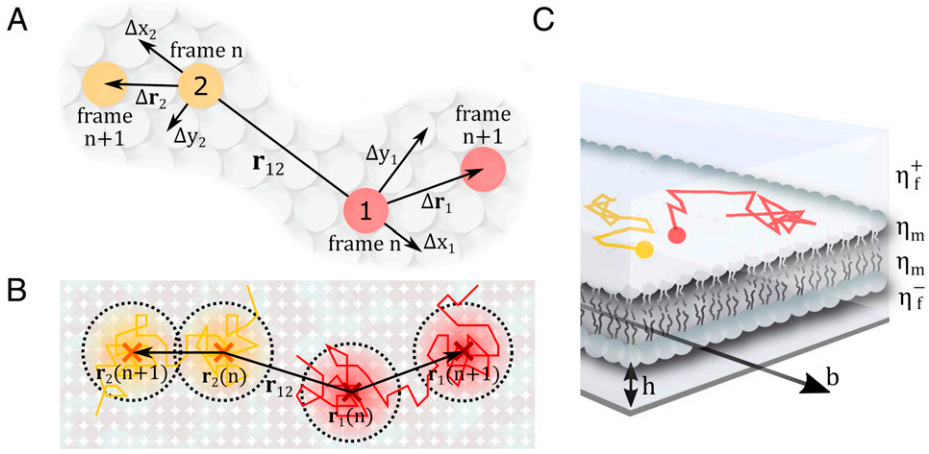

Fig. 3. Correlated Brownian motion in lipid bilayers. (*A*) Lipid motion in the coordinate system where the *x* axis is defined by the vector connecting the lipid pair $\boldsymbol{r}_{12}$. The probes $\ell = 1, 2$ move with displacements $\Delta \boldsymbol{r}_\ell = [\Delta x_\ell, \Delta y_\ell]$ during the time interval Δt. (*B*) Random trajectories of the probes showing the positions sampled during the finite illumination times Δt_{on} (indicated by the circles). The experimental detection only reveals the center of mass positions $\boldsymbol{r}_\ell(t)$ (indicated by the crosses). It is these averaged positions that are registered experimentally to create the trajectories. (*C*) Bilayer model used in the RS calculations. The parameters entering the model are the distance of the membrane to the support *h*, the surface viscosity for a leaflet η_m, the fluid viscosity of the aqueous superphase (subphase) η_f^+, and the interleaflet friction coefficient *b*.

thin fluid sheets (the monolayers), each with surface viscosity η_m, which slide against each another with an intermonolayer friction coefficient b. The monolayers are coupled to the surrounding bulk fluids via no-slip boundary conditions. These bulk fluids may have different viscosities above (η_f^+) and below (η_f^-) the bilayer. Diffusing lipids are assumed to have a radius R. For SLBs the separation distance between membrane and the underlying support h is finite, but it is infinite for the BLMs. In the traditional SD model, the membrane is represented by a single thin sheet (the bilayer) bounded on both sides by infinite fluids that share the same viscosity. (The present model reduces to SD in the limit where $b \to \infty$, $h \to \infty$ and $\eta_f^+ = \eta_f^-$. The infinite friction forces the monolayers to move in lockstep, resulting in a single sheet with a bilayer viscosity η_b=2η_m.) $R = 0.5$ nm (36), $\eta_f^+ = 0.001$ Pa s [bulk water value (37)], and $h = 1$ nm [for SLB cases (38, 39); $h = \infty$ for BLM cases] will be assumed throughout this work. The remaining parameters vary from system to system and will be discussed further in *Results*. Since $R = 0.5$ nm is adopted for both lipid probes, $D_1^\alpha = D_2^\alpha$ is enforced within the modeling, in agreement with the experimental findings of *Measuring and Analyzing Lipid Motion*.

Unfortunately, the two-leaflet approach does not yield analytical predictions for the dynamics of objects within the membrane [unlike the traditional single-sheet SD model, which does lead to analytical predictions (5, 10)]. Rather, it is necessary to perform numerical calculations to predict elements of the mobility/diffusion matrix (32, 40) and related quantities. The regularized Stokeslets (RS) (41, 42) technique has been used in this study to generate the diffusion matrix $\boldsymbol{D}(\boldsymbol{r}_{12})$; full details are available in refs. 18, 31, 33, and *SI Appendix*, *RS Calculations* provides a brief overview. For the present discussion, it suffices to recognize that the RS approach solves boundary value problems associated with particulate suspensions in the creeping flow hydrodynamic regime by treating the entire system (fluids and embedded particles) as fluid-like but with additional geometric constraints that impose rigid-body motion on those portions of the fluid associated with particles. This approach provides potentially exact solutions to the relevant hydrodynamic equations but is limited in practice by discretization issues. The calculations performed in this work were converged to an error of 2% or less.

As mentioned above, Eq. **1a** holds true for arbitrary $\Delta\tau$, but Eqs. **1b** and **1c** are restricted to the limit of small $\Delta\tau$. Unfortunately, even the short experimental pulses and intervals discussed above are far too long to allow an elementary data analysis based on Eqs. **1b** and **1c**. The experimental measurements reflect an inherent averaging of $\boldsymbol{r}_{12}$ during the Δt_{on} pulses and considerable changes in $\boldsymbol{r}_{12}$ during the Δt displacement interval. Finite-time correlations analogous to those in Eqs. **1b** and **1c** can be defined as

$$s_L^\alpha(A) \equiv \frac{\langle (\mathbb{X}_1)(\mathbb{X}_2 - A)\rangle}{2\Delta t}, \qquad [3a]$$

$$s_T^\alpha(A) \equiv \frac{\langle \mathbb{Y}_1 \mathbb{Y}_2\rangle}{2\Delta t}, \qquad [3b]$$

where

$$\mathbb{X}_\ell = \frac{1}{\Delta t_{on}}\int_{\Delta t_{on}+\Delta t_{off}}^{2\Delta t_{on}+\Delta t_{off}} dt\, x_\ell(t); \quad \mathbb{Y}_\ell = \frac{1}{\Delta t_{on}}\int_{\Delta t_{on}+\Delta t_{off}}^{2\Delta t_{on}+\Delta t_{off}} dt\, y_\ell(t) \qquad [4]$$

are the time-averaged lipid positions over the second pulse and the angular bracket average is understood to include only the subensemble of equilibrium systems with the following time-averaged positions over the first pulse:

$$\frac{1}{\Delta t_{on}}\int_0^{\Delta t_{on}} dt\, x_2(t) = A, \qquad [5]$$

$$\frac{1}{\Delta t_{on}}\int_0^{\Delta t_{on}} dt\, x_1(t) = \frac{1}{\Delta t_{on}}\int_0^{\Delta t_{on}} dt\, y_1(t) = \frac{1}{\Delta t_{on}}\int_0^{\Delta t_{on}} dt\, y_2(t) = 0. \qquad [6]$$

Here A plays a role analogous to r_{12}, but it is critical to recognize that A reflects an averaged lipid separation over the entire first pulse. The constraints in Eqs. **5** and **6** serve to define the x axis as the direction of longitudinal displacement, as in Fig. 3*A*, with a first-pulse averaged lipid–lipid separation A. (The centering of lipid one at the origin is arbitrary but convenient.) The $s_{L(T)}^\alpha(A)$ notation facilitates comparison with $D_{L(T)}^\alpha(r_{12})$ and $c_{L(T)}^\alpha(r_{12})$ below. Unlike $D_{L(T)}^\alpha(r_{12})$, $s_{L(T)}^\alpha(A)$ is well suited for direct experimental comparison. The $s_{L(T)}^\alpha(A)$ curves can be generated by Brownian dynamics simulations using the separation-dependent RS-generated diffusion matrix, $\boldsymbol{D}(\boldsymbol{r}_{12})$, for the evolution. However, this procedure is cumbersome when simulations must be repeatedly run to fit experimental data to hydrodynamic parameters. In practice, Eqs. **3a** and **3b** were calculated via a linear-response formalism, treating the correlation elements of the diffusion matrix as perturbations to independent diffusion by the two lipids. It was verified that this procedure yields good agreement with full Brownian dynamics simulations (43) for the range of parameters studied in this work; further details are provided in *SI Appendix*, *Brownian Dynamics Simulations* and *Linear Response Formalism*.

Correlated Motion in BLMs. The diffusive trajectories collected for Atto647N-DMPE and Atto550-DMPE in BLM_h and BLM_d were used to determine experimental correlations according to Eq. **2**. As above, fluorescence was quenched in one leaflet, and the analysis applies only to probe pairs occupying the same leaflet.

The correlations $c_L(r_{12})$ and $c_T(r_{12})$ for BLM_d are shown in Fig. 4 *A* and *B*, while the correlations $c_L(r_{12})$ and $c_T(r_{12})$ for BLM_h are shown in Fig. 4 *C* and *D*, respectively. The longitudinal correlation $c_L(r_{12})$ is positive at short distances and then decays with interparticle distance r_{12} over the μm scale for both BLMs, whereas the transverse correlation $c_T(r_{12})$ demonstrates only a weak positive signal for BLM_d and is immeasurably small over the whole range for BLM_h. The two free hydrodynamic parameters in the BLM geometry available for fitting are the interleaflet drag, b, and the monolayer viscosity, η_m. (Note that $\eta_f^- = \eta_f^+ = 0.001$ Pa s for the BLM systems.) These parameters were simultaneously fit to the mean lipid self-diffusion coefficient, $D = (D_1 + D_2)/2$ (via RS calculations) and to both correlation curves, $c_{L(T)}(r_{12})$ [via comparison to $s_{L(T)}(r_{12})$]. The fitting procedure is detailed in *SI Appendix*, *Fitting of Correlated Motion*. For BLM_d, the best-fit parameters (and associated 68% confidence intervals) are $\eta_m = 8 \times 10^{-11}$ Pa s m (7.6 to 8.2×10^{-11} Pa s m) and $b = 1.8 \times 10^3$ Pa s/m (4.2×10^2 to 1×10^4 Pa s/m). The best-fit diffusion matrix elements $D_L(r_{12})$ and $D_T(r_{12})$ are shown in Fig. 4 *A* and *B*, respectively, together with the corresponding time-averaged forms $s_L(r_{12})$ and $s_T(r_{12})$. The value obtained for the leaflet viscosity agrees well with a previous measurement of membrane viscosity for a BLM formed from a solution of similar lipids in *n*-dodecane (21). For BLM_h, the available correlation data provide insufficient information to convincingly guide the fit. (The data quality for BLM_h and BLM_d are comparable; however, BLM_h involves a more challenging parameter regime.) If it is assumed that the leaflet viscosity of BLM_h is the same as that of BLM_d (i.e., $\eta_m = 8 \times 10^{-11}$ Pa s m), then $b = 1.8 \times 10^7$ Pa s/m can be inferred solely from the self-diffusion numbers. This higher b value (consistent with lipid bilayers devoid of cosolvent) strongly couples the two leaflets together and causes the membrane to behave largely as a traditional SD single-sheet membrane with $L_{SD} = 2\eta_m/2\eta_f \approx 80$ nm. Predicted diffusion elements $D_L(r_{12})$ and $D_T(r_{12})$ assuming these values for η_m and b are shown in Fig.

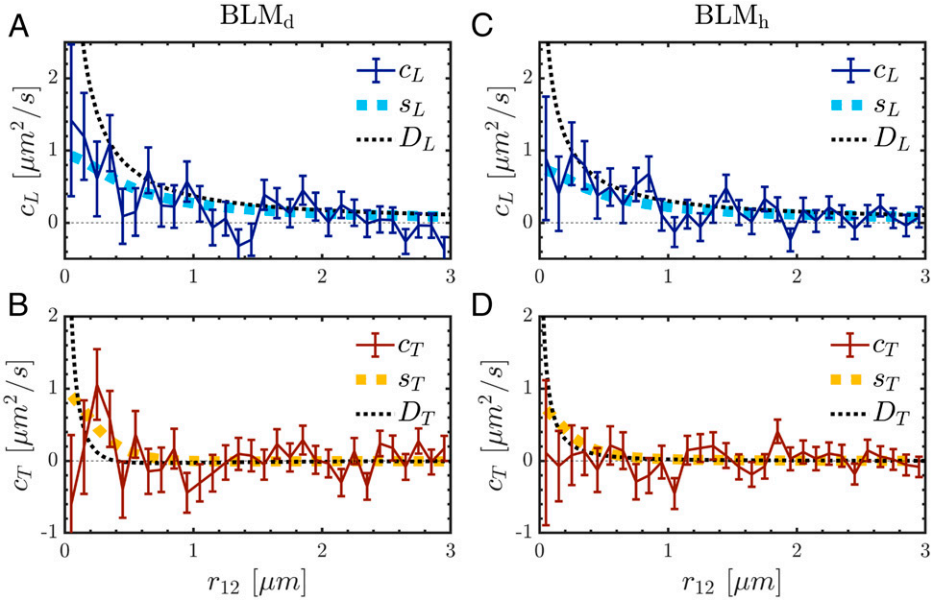

Fig. 4. Correlated Brownian motion as a function of distance r_{12} for BLMs and comparison with hydrodynamic theory. The panels show the experimental correlation functions, c_L or c_T (continuous line with error bars), as well as coupling diffusion coefficients calculated using the hydrodynamic theory, D_L or D_T (black dotted line), and the corresponding time-averaged forms, s_L or s_T (bold, colored dotted line). (*A* and *B*) BLM_d. (*C* and *D*) BLM_h.

4 *C* and *D*, respectively, together with the corresponding time-averaged forms $s_L(r_{12})$ and $s_T(r_{12})$. Although these curves rely on an assumed value of η_m, as opposed to fitting both free parameters independently, they appear consistent with the experimental data.

Lack of Correlations in SLBs. In the case of the SLB, probe behaviors in the distal and proximal leaflets differ drastically, as evidenced by the self-diffusion coefficients. The experimental correlations for the SLB in the distal leaflet, $c_L^+(r_{12})$ and $c_T^+(r_{12})$, are shown in Fig. 5 *A* and *B*, respectively, while the related correlations for the proximal leaflet, $c_L^-(r_{12})$ and $c_T^-(r_{12})$, are shown in Fig. 5 *C* and *D*. To within the experimental resolution, no detectable correlations are observed, unlike the case of the BLMs.

In the SLB geometry, there are in principle three hydrodynamic parameters available for fitting: η_m, b, and η_f^-. However, as in the case of BLM_h, the available correlation data are not helpful in determining these parameters. Adopting the value $\eta_m = 8 \times 10^{-11}$ Pa s m, as determined for BLM_d, and fitting to the ± self-diffusion coefficients using the RS method yields $b = 7.3 \times 10^7$ Pa s/m and $\eta_f^- = 7.3$ Pa s. This analysis suggests that

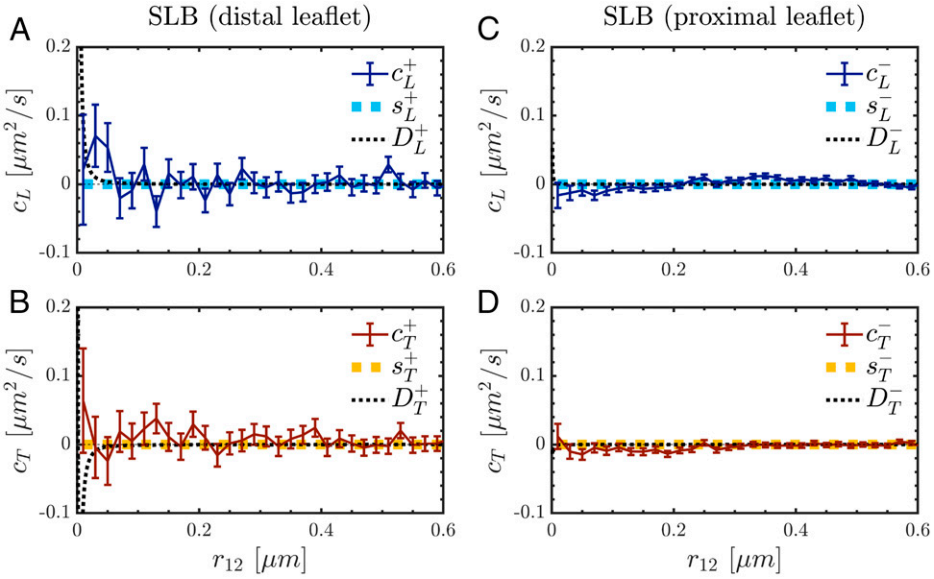

Fig. 5. Correlated Brownian motion as a function of distance r_{12} for an SLB and comparison with hydrodynamic theory. Each panel shows experimental correlations, c_L^α or c_T^α (continuous line with error bars), as well as the coupling diffusion coefficients calculated using hydrodynamic theory, D_L^α or D_T^α (black dotted line), and the corresponding time-averaged forms, s_L^α or s_T^α (colored dotted line), respectively. (*A* and *B*) Distal leaflet. (*C* and *D*) Proximal leaflet. While the predicted coupling diffusion coefficients are nonzero in a very narrow window close to $r_{12} = 0$, this is completely washed out by time averaging; the experiments correspondingly display no evidence of correlations.

the interleaflet friction is slightly larger than the BLM_h case, and the subphase viscosity is nearly four orders of magnitude larger than the viscosity of bulk water (0.001 Pa s) (37). The coupled diffusion coefficients, $D_L^{\alpha}(r_{12})$ and $D_T^{\alpha}(r_{12})$, and corresponding pulse-averaged quantities, $s_L^{\alpha}(r_{12})$ and $s_T^{\alpha}(r_{12})$, implied by these parameters are shown in Fig. 5. The theoretical predictions are barely visible on these axes, occurring only in the immediate vicinity of $r_{12} = 0$ for $D_{L(T)}^{\alpha}$, and that behavior is washed away upon pulse averaging. It is clear that the experimental uncertainties in r_{12} ($\langle \Delta r_{12}^2 \rangle^{1/2} \approx 150$ nm in the distal leaflet and $\langle \Delta r_{12}^2 \rangle^{1/2} \approx 50$ nm in the proximal leaflet), coupled with finite acquisition times, preclude measurement of hydrodynamic correlations in the supported geometry.

The qualitatively different behavior of the SLB correlations as compared to the BLMs is attributable to the large subphase viscosity, η_f^-, and small gap between membrane and support, $h = 1$ nm. In this regime, the substrate imparts a simple Evans–Sackmann-like (11) drag on the proximal leaflet with friction coefficient $b_{sub} = \frac{\eta_f^-}{h} = 7.3 \times 10^9$ Pa s/m (8, 18). As far as the distal leaflet is concerned, the proximal leaflet is largely locked in place by this strong friction. The interleaflet friction is two orders of magnitude smaller, so sliding motions predominately involve leaflet–leaflet slipping as opposed to leaflet–substrate slipping, and the distal leaflet behaves effectively as an Evans–Sackmann sheet above a support with effective friction coefficient $b_{eff} = b$. Hydrodynamic interactions in the distal leaflet are thus screened (8, 11, 18, 44) for separations exceeding $L_{sub} = \left(b/\eta_m^+\right)^{-1/2} = \sqrt{L_{SD}h} \approx 1$ nm. The range of interactions in the proximal leaflet is even smaller since there is no way to avoid the direct effect of b_{sub}. It is not surprising that hydrodynamic interactions cannot be detected, given the experimental resolution.

It is believed that some dyes interact directly with the glass substrate when incorporated into SLBs, leading to reduced dye diffusivities (45, 46). Thus, it might be tempting to attribute the small D^- values measured for the proximal leaflet of the SLB to dye molecules dragging on the substrate, as opposed to the elevated viscosity of trapped water suggested above. This mechanism was considered but was found to be inconsistent with the entirety of the data collected for the SLB system. To wit, if one assumes that the viscosity of water in the trapped layer is identical to that of bulk water (0.001 Pa s), it then proves impossible to reproduce the measured D^+ value for self-diffusion in the distal leaflet. (Even in the extreme limit of $b = \infty$, the predicted D^+ is too high.) Further, both probes used here are quite hydrophobic and naturally associate with membranes out of aqueous solution (47), so they are less likely to interact with the hydrophilic glass substrate than other common single-molecule labels (48). We cannot completely rule out the possibility of a hybrid mechanism, where both direct dye–substrate interactions and elevated η_f^- contribute to the observed measurements. However, this case introduces an additional unknown to the theoretical model (the direct friction on labels in the proximal leaflet), and it is impossible to uniquely determine the three free parameters (η_f^-, b, and direct probe friction) on the basis of the two available self-diffusion constants. No matter which mechanism is assumed (elevated η_f^- or a combination of elevated η_f^- and a direct probe interaction), it is always the case that the predicted correlations are too short-ranged to be measured experimentally, for any set of parameters capable of reproducing both D^- and D^+.

Discussion

Hydrodynamic interactions within lipid membranes can couple the motion of lipids or of proteins embedded in the membrane over distances much larger than the molecular scale. Collective motion in model lipid bilayers has been studied previously with neutron scattering experiments (49, 50) and molecular dynamics simulations (51, 52), but these methods could probe dynamics only over relatively short (nanometer) length scales. The present work avoids this limitation, allowing the study of distance-dependent correlated Brownian motion of lipid probes within membranes on the scale of hundreds of nanometers to microns. The study of both BLMs and SLBs highlights the considerable dynamical differences between these two systems, despite the fact that they were prepared with identical lipid mixtures. While self-diffusion in the distal leaflet in a SLB is reduced by a relatively modest amount (a factor of 3 to 5) relative to the BLMs, self-diffusion in the proximal leaflet is reduced by two orders of magnitude, and the μm-scale correlated motions seen in BLMs are completely suppressed (to within experimental resolution) in both SLB leaflets.

Two different BLMs were studied in this work. To understand the differences between them, it is important to review the BLM formation process (53). BLMs are formed over an aperture in a thin hydrophobic sheet from lipids dissolved in a nonpolar organic solvent, often a simple *n*-alkane (Fig. 1*B*). Following formation, the bilayer region remains in chemical equilibrium with a solvent annulus formed in the region of contact with the hydrophobic sheet, with some residual solvent partitioning into the bilayer. The partitioning of the hydrocarbon solvent in the bilayer region of BLMs is known to decrease with increasing chain length of the *n*-alkane (54). Indeed, capacitance measurements reveal that bilayers formed from lipids dissolved in *n*-decane are 62% thicker than solvent-free bilayers, whereas bilayers formed from lipids dissolved in *n*-hexadecane are only 10% thicker than the solvent-free case (55). X-ray diffraction, small-angle neutron scattering, and NMR measurements all suggest that the pronounced thickness increase of BLMs prepared with shorter-chain solvent is associated with the incorporation of solvent molecules into the region between the two leaflets (56–58). On the other hand, longer alkanes such as *n*-hexadecane predominately incorporate within the leaflets and align with the lipid chains, with a relatively low solubility of 1 solvent molecule per 6 to 10 lipid molecules (57).

Based on the differing modes of solvent partitioning, it is to be expected that the opposing leaflets in BLM_d should be coupled to each other more weakly than those in BLM_h, which should in turn be coupled more weakly than a solvent-free bilayer. Since the experimental data for BLM_h and the SLB cannot unambiguously assign values to both b and η_m, the value $\eta_m = 8 \times 10^{-11}$ Pa s m obtained from BLM_d has been assumed for the BLM_h and SLB cases. This choice is equivalent to the assumption that variations between BLM_h and BLM_d are due to changes in the interleaflet coupling, b. This view is affirmed by molecular dynamics simulations, which attribute the dominant effect on BLM properties to the solvent in the bilayer interior (59). A consistent picture emerges from this analysis, with the solvent-free SLB revealing the strongest interleaflet coupling, $b = 7.3 \times 10^7$ Pa s/m, followed by the nearly solvent-free BLM_h with $b = 1.8 \times 10^7$ Pa s/m and BLM_d with $b = 1.8 \times 10^3$ Pa s/m. Previously reported values for the interleaflet drag in solvent-free SLBs are in the range $b \approx 1 \times 10^7$ to 1×10^8 Pa s/m (60–62), in agreement with this analysis. It is worth noting that $b = 1.8 \times 10^3$ Pa s/m for BLM_d is quite low. One would naïvely predict $b \approx \eta/H \sim 5 \times 10^5$ Pa s/m for a 2-nm-thick layer ($H = 2$ nm) of *n*-decane ($\eta = 0.0009$ Pa s) (63), coupling the two monolayers together via no-slip boundary conditions on both sides. This discrepancy suggests a pronounced slipping between the *n*-decane layer and the two monolayers surrounding it.

In reality, and in contrast to the assumption above, slight differences in viscosity between BLM_d and BLM_h are probably to be expected. It is known, for example, that bilayer fluidity as measured using fluorescence anisotropy depends moderately on the *n*-alkane chain length (64). However, the viscosity of

BLM_h cannot differ drastically from $\eta_m = 8 \times 10^{-11}$ Pa s m. The correlation data for BLM_h may not allow for a full independent determination of η_m and b, but the range of possible viscosity values is only $\eta_m \approx (6 \text{ to } 14) \times 10^{-11}$ Pa s m, allowing for any possible b value between zero and infinity. These bounds are enforced solely by the self-diffusion measurements. The theoretical coupling diffusion coefficients $D_{L(T)}$ are then almost invariant over a relevant range of the possible viscosities η_m enforced by the self-diffusion measurements. This means, however, that despite the remaining uncertainty in η_m, the correct forms of the coupling diffusion coefficients $D_{L(T)}$ could still be obtained (*SI Appendix*, *Fitting of Correlated Motion*).

Turning to SLBs, several studies indicate differences in melting temperature T_m between the two leaflets. Atomic-force microscopy measurements have shown the existence of two independent structural phase transitions in SLBs, which were attributed to the independent melting of the two leaflets (65–68). It was correspondingly proposed that the interaction with the support modifies lipid order in the proximal leaflet. A recent neutron reflectometry study, however, revealed only minor leaflet asymmetry in the main melting transition due to the presence of the substrate (69). It is thus unclear whether the viscosities of the two leaflets should differ substantially in SLBs, and the answer may be very system dependent. In the absence of direct experimental guidance to the contrary, the same viscosity was assumed for both leaflets of the SLB. It follows that the substantial measured asymmetry in self-diffusion between the two leaflets requires a subphase viscosity larger by three to four orders of magnitude than that of bulk water (i.e., $\eta_f^- = 7.3$ Pa s). Viscosities larger by two to seven orders of magnitude from bulk water have previously been measured for interfacial water confined between surfaces (70, 71).

A key component of this study has been the deliberate attempt to compare experiment and hydrodynamic theory in a detailed and careful way for membrane systems. This proved to be somewhat more challenging than might be naively expected. The systems studied here (lipid probes in BLM and SLB geometries) break assumptions inherent to the well-known SD model. The required extensions to SD theory to account for two-leaflet dynamics do not yield closed-form analytical solutions. It is thus necessary to invoke numerical schemes to predict elements of the diffusion matrix for possible comparison to experimental measurements; RS calculations served this purpose in the present work. Unfortunately, molecular scale probes diffuse so rapidly that even the submillisecond acquisition times employed here yield data that are not suited for direct comparison to elements of the diffusion matrix. The $D_{L(T)}(r_{12})$ elements vary with probe positions, which are constantly evolving, and it is thus a time-averaged form of these quantities collected experimentally. The corresponding theoretical time averaging can be performed via Brownian dynamics simulations, using the RS-obtained diffusion matrix for the underlying dynamics, but this scheme is prohibitively expensive for the purposes of fitting parameters to the underlying hydrodynamic model. To accelerate this process, linear-response predictions have been derived and implemented numerically to allow for a direct comparison between experimental data and theoretical predictions. Under favorable circumstances, the resulting scheme (two-leaflet hydrodynamic theory → RS calculation of diffusion matrix → linear-response implementation of finite acquisition times→ fit to experimental data) allows for the extraction of all free parameters in the hydrodynamic model. This is the case for BLM_d. Unfortunately, the BLM_h and SLB cases involve parameter regimes that do not allow for unambiguous assignment of all relevant parameters based on the available experimental data. Future experiments might be able to resolve some of the ambiguities reported here, for example, by measuring correlations of particles that span both membrane leaflets.

The comparison between theory and experiment presented here indicates that SD-like hydrodynamic models are consistent with the collective Brownian motions of lipids in model membranes. To realize this correspondence, it is essential that the proper generalizations of SD hydrodynamics be employed and that theoretical predictions are crafted to correspond directly with experimental measurements. This is a point we have made previously, in the context of self-diffusion measurements (15, 18, 33). The present study extends this conclusion to correlated diffusion, which is a far more sensitive probe of hydrodynamic predictions than is self-diffusion.

What are the implications of the correlated motions in the membrane plane revealed here for membrane-related biological processes? It is known that hydrodynamic interactions can reduce diffusion-limited reaction rates (72, 73), and the effect is predicted to be especially strong in membranes (74). As observed here, the presence of a support hinders lipid flows relative to free membranes and screens the spatial extent of hydrodynamic interactions, hence potentially also affecting reactions in the membrane plane. Supporting structures such as the actin cytoskeleton are therefore likely to modulate membrane protein interactions by screening hydrodynamic flows. Due to the coupling of the two leaflets observed here, this effect would even translate to peripheral membrane proteins associated with the outer plasma membrane only (75, 76). Flow resistance in biological cells has been attributed primarily to momentum adsorption by immobile cytoskeleton-bound transmembrane proteins acting as direct obstacles for membrane flow (16, 30, 77, 78), while our results indicate that flow resistance may also result from supporting structures that influence the extracellular side of the membrane only indirectly.

Methods

See *SI Appendix* for a detailed description of the methodology for sample preparation, data collection, and analysis. Briefly, SLBs were prepared by allowing unilamellar vesicles to fuse on the surfaces of flow cells made of microscope cover glasses. The vesicles contained a small fraction of labeled lipids. BLMs were prepared by flowing a lipid *n*-alkane solution into a cell that contained a polymer sheet with a single wedge-shaped microaperture of a diameter of ~100 μm. Two-color single-molecule data were collected using a microscope in either total internal reflection mode (SLBs) or epi-illumination mode (BLMs), with pulsed illumination implemented as discussed in *Results*. Diffusive trajectories were obtained by localizing single molecules in individual camera frames and linking them in consecutive frames. The trajectories were then used to obtain correlated Brownian motion of probe pairs. Finally, the correlation data were analyzed using the RS technique, taking into account the time averaging due to finite camera acquisition times.

Data Availability. All study data are included in the article and/or *SI Appendix*.

ACKNOWLEDGMENTS. This work was supported in part by the Swiss National Science Foundation (Grants P300PA_174511 and P2BSP3_165336), the US–Israel Binational Science Foundation (Grant 2012084), and the NSF (Grant CHE-1800352). We thank Itay Barel for his Regularized Stokeslets code, which was used for the calculations in this paper, and Demian Lieberman for help with data collection. We also thank Prof. Haim Diamant for multiple discussions and encouragement.

1. R. B. Gennis, *Biomembranes: Molecular Structure and Function* (Springer-Verlag, 1989).
2. H. Lodish *et al.*, *Molecular Cell Biology* (Scientific American Books, New York, 1995).
3. R. Lipowsky, E. Sackmann, *Structure and Dynamics of Membranes* (Elsevier Science, 1995).
4. D. Nelson, T. Piran, S. Weinberg, *Statistical Mechanics of Membranes and Surfaces* (World Scientific, 2004).
5. P. G. Saffman, Brownian motion in thin sheets of viscous fluid. *J. Fluid Mech.* **73**, 593–602 (1976).
6. P. G. Saffman, M. Delbrück, Brownian motion in biological membranes. *Proc. Natl. Acad. Sci. U.S.A.* **72**, 3111–3113 (1975).
7. N. Oppenheimer, H. Diamant, Correlated diffusion of membrane proteins and their effect on membrane viscosity. *Biophys. J.* **96**, 3041–3049 (2009).

8. D. K. Lubensky, R. E. Goldstein, Hydrodynamics of monolayer domains at the air–water interface. *Phys. Fluids* **8**, 843–854 (1996).
9. M. Doi, S. F. Edwards, *The Theory of Polymer Dynamics* (Clarendon Press, 1986).
10. B. D. Hughes, B. A. Pailthorpe, L. R. White, The translational and rotational drag on a cylinder moving in a membrane. *J. Fluid Mech.* **110**, 349–372 (1981).
11. E. Evans, E. Sackmann, Translational and rotational drag coefficients for a disk moving in a liquid membrane associated with a rigid substrate. *J. Fluid Mech.* **194**, 553–561 (1988).
12. H. A. Stone, A. Ajdari, Hydrodynamics of particles embedded in a flat surfactant layer overlying a subphase of finite depth. *J. Fluid Mech.* **369**, 151–173 (1998).
13. N. Oppenheimer, H. Diamant, Correlated dynamics of inclusions in a supported membrane. *Phys. Rev. E Stat. Nonlin. Soft Matter Phys.* **82**, 041912 (2010).
14. E. Evans, A. Yeung, Hidden dynamics in rapid changes of bilayer shape. *Chem. Phys. Lipids* **73**, 39–56 (1994).
15. B. A. Camley, M. G. Lerner, R. W. Pastor, F. L. H. Brown, Strong influence of periodic boundary conditions on lateral diffusion in lipid bilayer membranes. *J. Chem. Phys.* **143**, 243113 (2015).
16. N. Oppenheimer, H. Diamant, In-plane dynamics of membranes with immobile inclusions. *Phys. Rev. Lett.* **107**, 258102 (2011).
17. U. Seifert, S. A. Langer, Viscous modes of fluid bilayer membranes. *Europhys. Lett.* **23**, 71–76 (1993).
18. B. A. Camley, F. L. H. Brown, Diffusion of complex objects embedded in free and supported lipid bilayer membranes: Role of shape anisotropy and leaflet structure. *Soft Matter* **9**, 4767–4779 (2013).
19. M. J. Saxton, K. Jacobson, Single-particle tracking: Applications to membrane dynamics. *Annu. Rev. Biophys. Biomol. Struct.* **26**, 373–399 (1997).
20. S. Ramadurai *et al.*, Lateral diffusion of membrane proteins. *J. Am. Chem. Soc.* **131**, 12650–12656 (2009).
21. K. Weiß *et al.*, Quantifying the diffusion of membrane proteins and peptides in black lipid membranes with 2-focus fluorescence correlation spectroscopy. *Biophys. J.* **105**, 455–462 (2013).
22. P. Cicuta, S. L. Keller, S. L. Veatch, Diffusion of liquid domains in lipid bilayer membranes. *J. Phys. Chem. B* **111**, 3328–3331 (2007).
23. Y. Gambin *et al.*, Lateral mobility of proteins in liquid membranes revisited. *Proc. Natl. Acad. Sci. U.S.A.* **103**, 2098–2102 (2006).
24. J. Kriegsmann *et al.*, Translational diffusion and interaction of a photoreceptor and its cognate transducer observed in giant unilamellar vesicles by using dual-focus FCS. *ChemBioChem* **10**, 1823–1829 (2009).
25. C. C. Lee, M. Revington, S. D. Dunn, N. O. Petersen, The lateral diffusion of selectively aggregated peptides in giant unilamellar vesicles. *Biophys. J.* **84**, 1756–1764 (2003).
26. T. T. Hormel, S. Q. Kurihara, M. K. Brennan, M. C. Wozniak, R. Parthasarathy, Measuring lipid membrane viscosity using rotational and translational probe diffusion. *Phys. Rev. Lett.* **112**, 188101 (2014).
27. J. C. Crocker *et al.*, Two-point microrheology of inhomogeneous soft materials. *Phys. Rev. Lett.* **85**, 888–891 (2000).
28. C. Cheung, Y. H. Hwang, Xl. Wu, H. J. Choi, Diffusion of particles in free-standing liquid films. *Phys. Rev. Lett.* **76**, 2531–2534 (1996).
29. V. Prasad, S. A. Koehler, E. R. Weeks, Two-particle microrheology of quasi-2D viscous systems. *Phys. Rev. Lett.* **97**, 176001 (2006).
30. M. Chein, E. Perlson, Y. Roichman, Flow arrest in the plasma membrane. *Biophys. J.* **117**, 810–816 (2019).
31. E. Noruzifar, B. A. Camley, F. L. H. Brown, Calculating hydrodynamic interactions for membrane-embedded objects. *J. Chem. Phys.* **141**, 124711 (2014).
32. S. Kim, S. J. Karrila, *Microhydrodynamics: Principles and Selected Applications* (Dover Publications, Mineola, NY, 2005).
33. R. L. Schoch, I. Barel, F. L. H. Brown, G. Haran, Lipid diffusion in the distal and proximal leaflets of supported lipid bilayer membranes studied by single particle tracking. *J. Chem. Phys.* **148**, 123333 (2018).
34. L. Xiang, K. Chen, R. Yan, W. Li, K. Xu, Single-molecule displacement mapping unveils nanoscale heterogeneities in intracellular diffusivity. *Nat. Methods* **17**, 524–530 (2020).
35. A. Honigmann, C. Walter, F. Erdmann, C. Eggeling, R. Wagner, Characterization of horizontal lipid bilayers as a model system to study lipid phase separation. *Biophys. J.* **98**, 2886–2894 (2010).
36. K. Graf, H. Riegler, Molecular adhesion interactions between Langmuir monolayers and solid substrates. *Colloids Surf. A Physicochem. Eng. Asp.* **131**, 215–224 (1998).
37. W. M. Haynes, D. R. Lide, T. J. Bruno, *CRC Handbook of Chemistry and Physics: A Ready-Reference Book of Chemical and Physical Data* (CRC Press, ed. 97, 2016).
38. C. M. Ajo-Franklin, C. Yoshina-Ishii, S. G. Boxer, Probing the structure of supported membranes and tethered oligonucleotides by fluorescence interference contrast microscopy. *Langmuir* **21**, 4976–4983 (2005).
39. T. J. Zwang, W. R. Fletcher, T. J. Lane, M. S. Johal, Quantification of the layer of hydration of a supported lipid bilayer. *Langmuir* **26**, 4598–4601 (2010).
40. J. Happel, H. Brenner, *Low Reynolds Number Hydrodynamics with Special Applications to Particulate Media* (Springer Netherlands, 1983).
41. R. Cortez, L. Fauci, A. Medovikov, The method of regularized Stokeslets in three dimensions: Analysis, validation, and application to helical swimming. *Phys. Fluids* **17**, 031504 (2005).
42. R. Cortez, The method of regularized Stokeslets. *SIAM J. Sci. Comput.* **23**, 1204–1225 (2001).
43. D. L. Ermak, J. A. McCammon, Brownian dynamics with hydrodynamic interactions. *J. Chem. Phys.* **69**, 1352–1360 (1978).
44. K. Seki, S. Mogre, S. Komura, Diffusion coefficients in leaflets of bilayer membranes. *Phys. Rev. E Stat. Nonlin. Soft Matter Phys.* **89**, 022713 (2014).
45. T. Otosu, S. Yamaguchi, Quantifying the diffusion of lipids in the proximal/distal leaflets of a supported lipid bilayer by two-dimensional fluorescence lifetime correlation spectroscopy. *J. Phys. Chem. B* **122**, 10315–10319 (2018).
46. X. Woodward, E. E. Stimpson, C. V. Kelly, Single-lipid tracking on nanoscale membrane buds: The effects of curvature on lipid diffusion and sorting. *Biochim. Biophys. Acta Biomembr.* **1860**, 2064–2075 (2018).
47. L. D. Hughes, R. J. Rawle, S. G. Boxer, Choose your label wisely: Water-soluble fluorophores often interact with lipid bilayers. *PLoS One* **9**, e87649 (2014).
48. H. Blom, K. Hassler, A. Chmyrov, J. Widengren, Electrostatic interactions of fluorescent molecules with dielectric interfaces studied by total internal reflection fluorescence correlation spectroscopy. *Int. J. Mol. Sci.* **11**, 386–406 (2010).
49. M. C. Rheinstädter *et al.*, Motional coherence in fluid phospholipid membranes. *Phys. Rev. Lett.* **101**, 248106 (2008).
50. S. Busch, C. Smuda, L. C. Pardo, T. Unruh, Molecular mechanism of long-range diffusion in phospholipid membranes studied by quasielastic neutron scattering. *J. Am. Chem. Soc.* **132**, 3232–3233 (2010).
51. G. S. Ayton, G. A. Voth, Mesoscopic lateral diffusion in lipid bilayers. *Biophys. J.* **87**, 3299–3311 (2004).
52. E. Falck, T. Róg, M. Karttunen, I. Vattulainen, Lateral diffusion in lipid membranes through collective flows. *J. Am. Chem. Soc.* **130**, 44–45 (2008).
53. H. T. Tien, A. Ottova-Leitmannova, *Planar Lipid Bilayers (BLMs) and Their Applications* (Elsevier Science, 2003).
54. S. H. White, "The physical nature of planar bilayer membranes" in *Ion Channel Reconstitution*, C. Miller, Ed. (Springer, Boston, MA, 1986), pp. 3–35.
55. L. C. M. Gross, A. J. Heron, S. C. Baca, M. I. Wallace, Determining membrane capacitance by dynamic control of droplet interface bilayer area. *Langmuir* **27**, 14335–14342 (2011).
56. J. M. Pope, L. W. Walker, D. Dubro, On the ordering of N-alkane and N-alcohol solutes in phospholipid bilayer model membrane systems. *Chem. Phys. Lipids* **35**, 259–277 (1984).
57. T. J. McIntosh, S. A. Simon, R. C. MacDonald, The organization of n-alkanes in lipid bilayers. *Biochim. Biophys. Acta* **597**, 445–463 (1980).
58. N. Kučerka *et al.*, Location of the general anesthetic n-decane in model membranes. *J. Mol. Liq.* **276**, 624–629 (2019).
59. V. Zoni, P. Campomanes, S. Vanni, Investigating the structural properties of hydrophobic solvent-rich lipid bilayers. *Soft Matter* **17**, 5329–5335 (2021).
60. P. Jönsson, J. P. Beech, J. O. Tegenfeldt, F. Höök, Mechanical behavior of a supported lipid bilayer under external shear forces. *Langmuir* **25**, 6279–6286 (2009).
61. S. R. Tabaei, J. J. J. Gillissen, N.-J. Cho, Probing membrane viscosity and interleaflet friction of supported lipid bilayers by tracking electrostatically adsorbed, nano-sized vesicles. *Small* **12**, 6338–6344 (2016).
62. R. Merkel, E. Sackmann, E. Evans, Molecular friction and epitactic coupling between monolayers in supported bilayers. *J. Phys.* (*Paris*) **50**, 1535–1555 (1989).
63. J. H. Dymond, H. A. Øye, Viscosity of selected liquid n-alkanes. *J. Phys. Chem. Ref. Data* **23**, 41–53 (1994).
64. G. D. Bothun, B. L. Knutson, H. J. Strobel, S. E. Nokes, Liposome fluidization and melting point depression by compressed and liquid n-alkanes. *Colloids Surf. A Physicochem. Eng. Asp.* **279**, 50–57 (2006).
65. A. Charrier, F. Thibaudau, Main phase transitions in supported lipid single-bilayer. *Biophys. J.* **89**, 1094–1101 (2005).
66. D. Keller, N. B. Larsen, I. M. Møller, O. G. Mouritsen, Decoupled phase transitions and grain-boundary melting in supported phospholipid bilayers. *Phys. Rev. Lett.* **94**, 025701 (2005).
67. Z. V. Feng, T. A. Spurlin, A. A. Gewirth, Direct visualization of asymmetric behavior in supported lipid bilayers at the gel-fluid phase transition. *Biophys. J.* **88**, 2154–2164 (2005).
68. H.-L. Wu, Y. Tong, Q. Peng, N. Li, S. Ye, Phase transition behaviors of the supported DPPC bilayer investigated by sum frequency generation (SFG) vibrational spectroscopy and atomic force microscopy (AFM). *Phys. Chem. Chem. Phys.* **18**, 1411–1421 (2016).
69. Y. Gerelli, Phase transitions in a single supported phospholipid bilayer: Real-time determination by neutron reflectometry. *Phys. Rev. Lett.* **122**, 248101 (2019).
70. R. C. Major, J. E. Houston, M. J. McGrath, J. I. Siepmann, X.-Y. Zhu, Viscous water meniscus under nanoconfinement. *Phys. Rev. Lett.* **96**, 177803 (2006).
71. D. Ortiz-Young, H.-C. Chiu, S. Kim, K. Voïtchovsky, E. Riedo, The interplay between apparent viscosity and wettability in nanoconfined water. *Nat. Commun.* **4**, 1–6 (2013).
72. J. M. Deutch, B. U. Felderhof, Hydrodynamic effect in diffusion-controlled reaction. *J. Chem. Phys.* **59**, 1669–1671 (1973).
73. D. F. Calef, J. M. Deutch, Diffusion-controlled reactions. *Annu. Rev. Phys. Chem.* **34**, 493–524 (1983).
74. N. Oppenheimer, H. A. Stone, Effect of hydrodynamic interactions on reaction rates in membranes. *Biophys. J.* **113**, 440–447 (2017).
75. C. Zurzolo, K. Simons, Glycosylphosphatidylinositol-anchored proteins: Membrane organization and transport. *Biochim. Biophys. Acta* **1858**, 632–639 (2016).
76. D. Goswami *et al.*, Nanoclusters of GPI-anchored proteins are formed by cortical actin-driven activity. *Cell* **135**, 1085–1097 (2008).
77. Z. Shi, Z. T. Graber, T. Baumgart, H. A. Stone, A. E. Cohen, Cell membranes resist flow. *Cell* **175**, 1769–1779.e13 (2018).
78. A. E. Cohen, Z. Shi, Do cell membranes flow like honey or jiggle like jello? *BioEssays* **42**, e1900142 (2020).